

Cite this: *RSC Adv.*, 2018, 8, 34525

A comparison of TiF_3 and NbF_5 catalytic effects on hydrogen absorption and desorption kinetics of a ball-milled $\text{Mg}_{85}\text{Zn}_5\text{Ni}_{10}$ alloy

Yi Yin,^a Bo Li,^a Zeming Yuan,^{*ab} Yan Qi^a and Yanghuan Zhang^{id} ^{*ab}

In this investigation, the as-milled $\text{Mg}_{85}\text{Zn}_5\text{Ni}_{10}\text{-4C}$ ($\text{C} = \text{TiF}_3, \text{NbF}_5$) composites were successfully produced via ball milling. The different influences between the catalysts TiF_3 and NbF_5 on the hydrogen storage behavior and microstructure of the composites were investigated by XRD, SEM, TEM and hydrogen absorption/desorption tests. The as-milled $\text{Mg}_{85}\text{Zn}_5\text{Ni}_{10}\text{-4C}$ ($\text{C} = \text{TiF}_3, \text{NbF}_5$) alloys contain the major phase Mg, the secondary phase Mg_2Ni , a small amount of MgZn_2 , TiF_3 and NbF_5 . After hydrogenation, MgH_2 and Mg_2NiH_4 are formed, which convert back into Mg and Mg_2Ni after dehydrogenation indicating that MgZn_2 and the catalysts TiF_3 and NbF_5 do not react with hydrogen. Compared with NbF_5 catalyzed alloy, the TiF_3 catalyzed alloy has a faster hydrogen absorption/desorption kinetics. On the basis of Arrhenius equation, the dehydrogenation activation energy values of the as-milled $\text{Mg}_{85}\text{Zn}_5\text{Ni}_{10}\text{-4C}$ ($\text{C} = \text{TiF}_3, \text{NbF}_5$) alloys are 75.514 and 82.367 $\text{kJ mol}^{-1} \text{H}_2$, respectively, while the value of ball-milled $\text{Mg}_{85}\text{Zn}_5\text{Ni}_{10}$ alloy is 109.830 $\text{kJ mol}^{-1} \text{H}_2$. As a result, both TiF_3 and NbF_5 can significantly ameliorate the hydrogen storage thermodynamics. TiF_3 shows better catalytic influence on hydrogen storage property of $\text{Mg}_{85}\text{Zn}_5\text{Ni}_{10}$ than NbF_5 .

Received 2nd August 2018
Accepted 22nd September 2018

DOI: 10.1039/c8ra06500d

rsc.li/rsc-advances

Introduction

For nearly half a century, rapid economic development and energy crisis have threatened our existence because of excessive exploitation of non-renewable energy sources. Meanwhile, the consequent environmental problems arising from the excessive use of fossil fuels are becoming increasingly prominent. There is a growing demand for a new kind of renewable energy. Therefore, many scholars pay attention to hydrogen owing to its high efficiency, environment friendly nature, and renewable characteristics.^{1–13} However, the problem that is severely restricting the application of hydrogen is availability of a safe and credible storage mode.^{14–16} Because of the merits of high gravimetric storage density and safety, many researchers have great expectations from metal hydrides as a hydrogen storage material.^{15–20} Most researchers believe that among the different metals which can form hydrides, Mg is the most potential candidate to be widely used as a hydrogen storage material because of its low price, excellent reversibility, abundance, and high gravimetric hydrogen storage densities (7.6 wt%).^{21,22} However at the same time, the inherent shortcomings of Mg, such as the high decomposition temperature of its hydride and poor storage kinetics seriously impede its commercial

development. Therefore, it is essential to ameliorate the kinetics and thermodynamics of the hydrogen storage alloys.

Some researches have confirmed that alloying Mg with transition metals such as Ni,^{23–25} Zn,^{26,27} Ti, Cr, Nb, Cu and Fe^{28–31} can enhance the hydrogenation/dehydrogenation rates. Also, some rare earth elements,^{32–34} intermetallic compounds,³⁵ metallic oxides,^{36,37} and fluorides^{38–40} are proven to have a good catalytic effect on accelerating the storage and release of hydrogen. Yavari *et al.*⁴¹ added FeF_3 into MgH_2 to manufacture nanostructured MgH_2 composites and found that hydrogenation/dehydrogenation rates were clearly enhanced. Lee *et al.*⁴² synthesized Mg–5NbF₅ and showed that Mg–5NbF₅ had faster initial hydrogen absorption and desorption and a larger effective storage capacity. Ma *et al.*³⁹ mechanically prepared a $\text{MgH}_2 + \text{TiF}_3$ system and proved that mechanical milling with 4 mol% TiF_3 could enhance the sorption kinetics markedly and reduce operation temperatures in particular. The hydrogenation could be accomplished in about 25 s even at 313–373 K. Recham *et al.*⁴³ showed that NbF_5 could reduce the dehydrogenation temperature while enhancing the kinetics of ball-milled MgH_2 with 2 mol% of NbF_5 as the optimum concentration. It is believed that the transition metal fluorides play a key role in enhancing the hydrogenation kinetics of Mg.⁴²

In this study, we designed a new kind of Mg based $\text{Mg}_{85}\text{Zn}_5\text{Ni}_{10}$ ternary alloy, and ball milled it with TiF_3 and NbF_5 as catalysts to ameliorate the hydrogen storage properties. We also thoroughly investigated the influence of doping TiF_3 and NbF_5 on the microstructure and hydrogen storage performances of experimental materials. The storing and releasing characteristics and activation energies were also analysed.

^aDepartment of Functional Material Research, Central Iron and Steel Research Institute, Beijing 100081, China. E-mail: zhangyh59@sina.com; zmyuan153@163.com

^bKey Laboratory of Integrated Exploitation of Baiyun Obo Multi-Metal Resources, Inner Mongolia University of Science and Technology, Baotou 014010, China

Experimental

Mg₈₅Zn₅Ni₁₀ alloy was prepared using a vacuum induction furnace under 0.04 MPa helium atmosphere. Extra 10 wt% Mg was added to reduce the volatilization of magnesium during melting. The as-cast alloy ingots were mechanically crushed into powders (particle size < 75 μm). Then the as-cast alloy powder was mixed with 4 wt% TiF₃ and NbF₅ and transferred to a mechanical ball mill. A planetary-type mill was used under an Ar atmosphere for milling. The weight ratio of the alloy powder and Cr–Ni stainless steel balls was 1 : 40. The milling speed was 350 rpm. During ball milling, in order to prevent excess heating, the mill was set to rest for 1 h after every 1 h of working. The samples were milled for a total of 5 h. The as-milled Mg₈₅Zn₅Ni₁₀ + 4 wt% C (C = TiF₃ and NbF₅) in this research are named as Mg₈₅Zn₅Ni₁₀–4C (C = TiF₃, NbF₅). Phase structures, morphologies and crystalline states of the ball-milled Mg₈₅Zn₅Ni₁₀ + 4 wt% C (C = TiF₃ and NbF₅) alloys were investigated and observed by X-ray diffraction (XRD) (D/max/2400), SEM and high resolution transmission electron microscopy (HRTEM) (JEM-2100F).

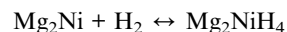
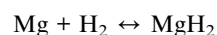
A Sieverts-type apparatus was used to measure the pressure–composition isotherms (P–C–I) and hydrogen absorption/desorption kinetics. First, 6 hydrogen absorption and desorption cycles were performed at 360 °C to completely activate the samples. PCI curves were tested at 360, 340 and 320 °C. The hydrogen absorption was conducted at a hydrogen pressure of 3 MPa, at 360, 340, 320, 300, 280, 260, 240, 220, 200 and 150 °C respectively. The hydrogen desorption was tested at a pressure of 1×10^{-4} MPa at 360, 340, 320, 300 and 280 °C.

The dehydrogenation process of the ball-milled Mg₈₅Zn₅Ni₁₀ + 4 wt% C (C = TiF₃ and NbF₅) alloys was studied by differential scanning calorimetry (DSC) on a NETZSCH, STA 449F3 instrument. The flow rate of argon was 50 mL min^{−1}. The hydrogen saturated-samples were gradually heated from room temperature to 500 °C with an increase of 5 °C min^{−1}.

Results and discussion

Phase and microstructural characteristics

X-ray diffraction (XRD) has been utilized in studying the phase compositions and structures of ball-milled Mg₈₅Zn₅Ni₁₀ and Mg₈₅Zn₅Ni₁₀–4C (C = TiF₃, NbF₅) before and after hydrogen absorption/desorption, as described in Fig. 1. We can see that after 5 h ball milling, the broadened diffraction peaks reveal that mechanical ball milling causes the reduction of grain size and amorphization. According to Fig. 1, the ball-milled Mg₈₅Zn₅Ni₁₀ contains three phases: Mg as the major phase, the secondary phase Mg₂Ni, and a small MgZn₂ phase. Meanwhile, after adding TiF₃ and NbF₅, no new phase appeared in the XRD curves, indicating no reaction occurred between the catalysts TiF₃ and NbF₅ and Mg₈₅Zn₅Ni₁₀ during ball milling. Mg and Mg₂Ni are still the major and the secondary phase in Mg₈₅Zn₅Ni₁₀–4C (C = TiF₃, NbF₅) alloys, respectively. After hydrogen absorption, it is clear that the Mg phase is converted into MgH₂. Simultaneously, Mg₂Ni converts to Mg₂NiH₄. It is worth noting that among all three samples, only MgZn₂ existed after hydrogen absorption, showing that it does not react with hydrogen. After hydrogen desorption, MgH₂ and Mg₂NiH₄ change into Mg and Mg₂Ni, respectively. MgZn₂ is also found in the dehydrogenated alloys. Based on the XRD patterns, there are two reversible reactions for hydrogenation and dehydrogenation of the alloys. The reaction path ways can be inferred as follows:



The Mg₈₅Zn₅Ni₁₀–4C (C = TiF₃, NbF₅) alloy samples after hydrogen absorption and desorption were detected by HRTEM and ED, as described in Fig. 2. After ball milling with the

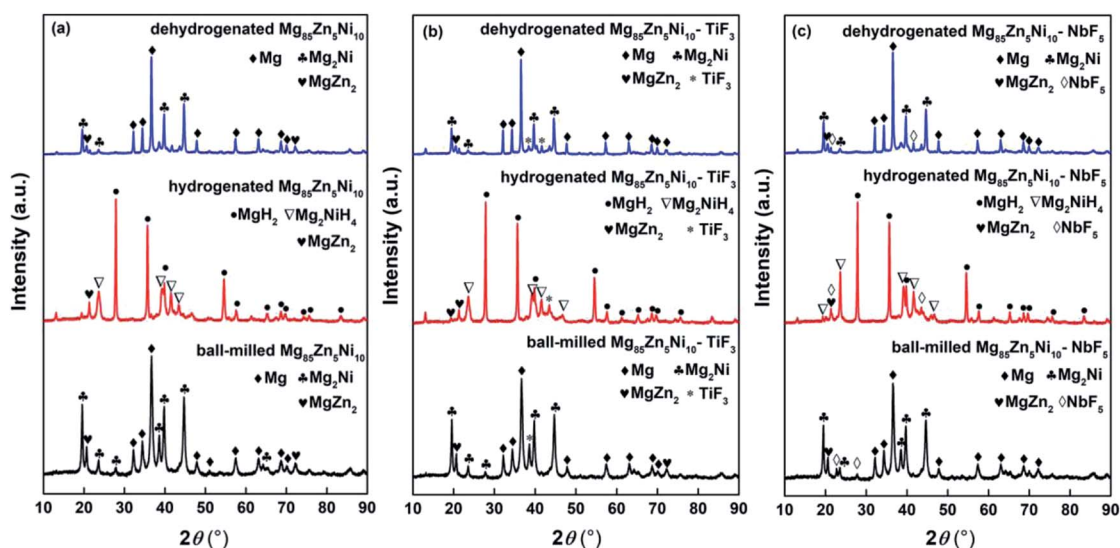


Fig. 1 XRD patterns of the ball-milled Mg₈₅Zn₅Ni₁₀ and Mg₈₅Zn₅Ni₁₀–4C (C = TiF₃, NbF₅) alloys before and after 30 hydrogen absorption and desorption cycles: (a) ball-milled, (b) C = TiF₃, (c) C = NbF₅.



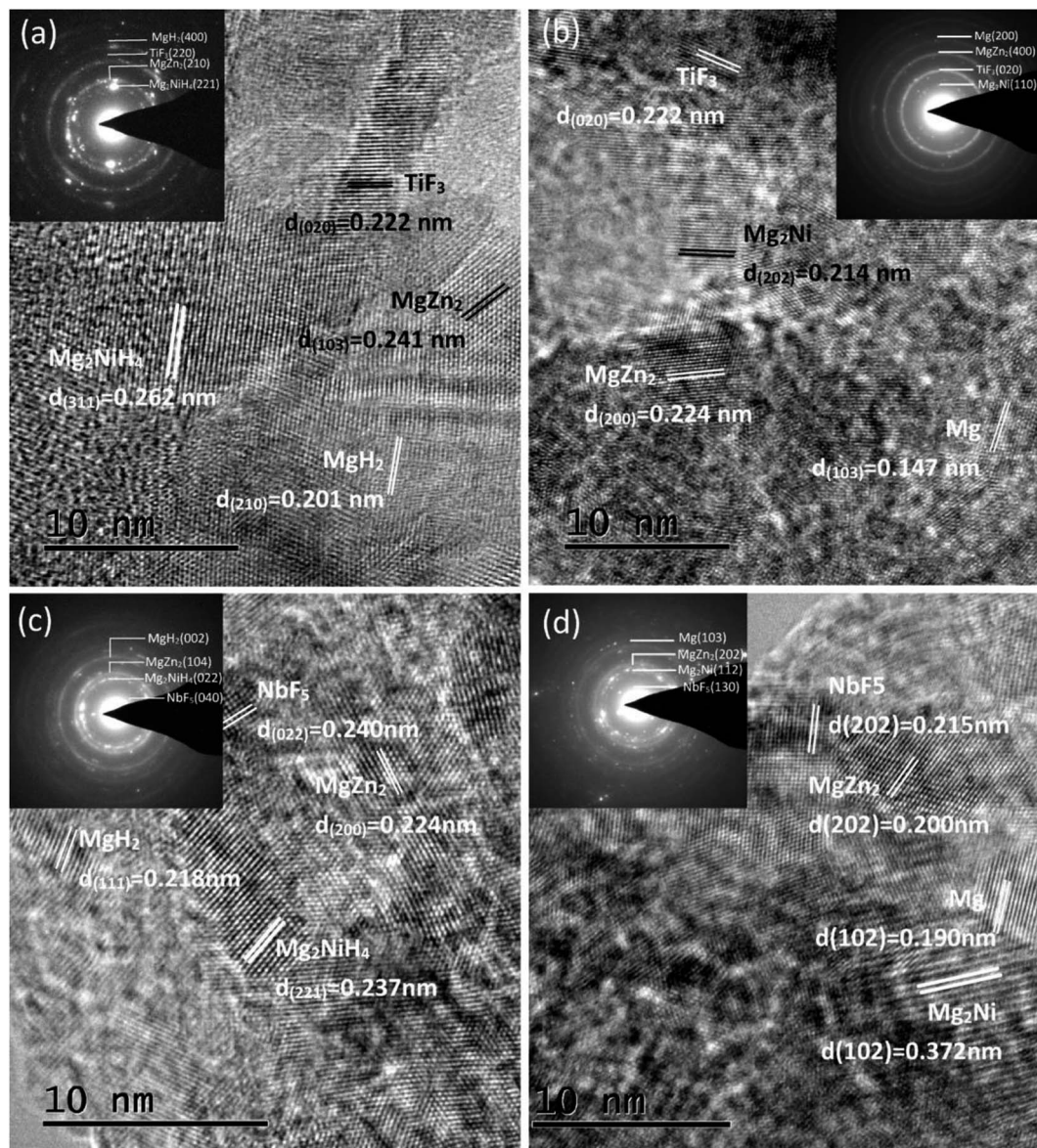


Fig. 2 HRTEM micrographs and SAED patterns of the $\text{Mg}_{85}\text{Zn}_5\text{Ni}_{10}\text{-}4\text{C}$ ($\text{C} = \text{TiF}_3, \text{NbF}_5$) alloys after hydrogen absorption and desorption: (a) hydrogenated $\text{C} = \text{TiF}_3$, (b) dehydrogenated $\text{C} = \text{TiF}_3$, (c) hydrogenated $\text{C} = \text{NbF}_5$, (d) dehydrogenated $\text{C} = \text{NbF}_5$.

catalysts and hydrogen absorption and desorption, partial nanocrystalline and amorphous phases form in the $\text{Mg}_{85}\text{Zn}_5\text{Ni}_{10}\text{-}4\text{C}$ ($\text{C} = \text{TiF}_3, \text{NbF}_5$) alloys. Evidently, after hydrogen absorption, $\text{Mg}_{85}\text{Zn}_5\text{Ni}_{10}\text{-}4\text{TiF}_3$ contains MgH_2 , Mg_2NiH_4 , MgZn_2 and TiF_3 phases, and $\text{Mg}_{85}\text{Zn}_5\text{Ni}_{10}\text{-}4\text{NbF}_5$ possesses MgH_2 , Mg_2NiH_4 , MgZn_2 and NbF_5 phases, which are sustained through ED patterns and also consistent with the XRD test. According to the structural analysis and index of ED rings, MgH_2 and Mg_2NiH_4 convert into Mg and Mg_2Ni respectively. MgZn_2 , TiF_3 and NbF_5 are found after hydrogen desorption, suggesting absence of reaction among MgZn_2 , TiF_3 , NbF_5 and hydrogen. The catalysts TiF_3 and NbF_5 exist stably in the $\text{Mg}_{85}\text{Zn}_5\text{Ni}_{10}\text{-}4\text{C}$ ($\text{C} = \text{TiF}_3, \text{NbF}_5$) composites after ball milling, even after 30 hydrogenation and dehydrogenation cycles. The results of HRTEM and ED coincide with the XRD results.

Fig. 3 and 4 present the bright field FETEM images and EDS mapping of the $\text{Mg}_{85}\text{Zn}_5\text{Ni}_{10}\text{-}4\text{TiF}_3$ and $\text{Mg}_{85}\text{Zn}_5\text{Ni}_{10}\text{-}4\text{NbF}_5$ alloys after dehydrogenation cycles, respectively. The different colours express the distributions of different elements. As can be seen from Fig. 3(a) and (b), Mg is the major component covering the main matrix of a single $\text{Mg}_{85}\text{Zn}_5\text{Ni}_{10}\text{-}4\text{TiF}_3$ alloy particle. In Fig. 3(c) and (d), the Ni and Zn elements are mainly distributed in the bright regions of the alloy particle illustrating that Mg-Ni and Mg-Zn metal compounds are distributed on the surface of the alloy particle. The Ti and F elements are relatively well-distributed around the alloy particle indicating uniform inlaying of TiF_3 on Mg matrix which is corroborated by XRD and TEM results. Similarly, according to Fig. 4, Nb and F elements are also well-distributed on the $\text{Mg}_{85}\text{Zn}_5\text{Ni}_{10}\text{-}4\text{NbF}_5$ alloy particles. Based on XRD, TEM and EDS mapping, the catalysts



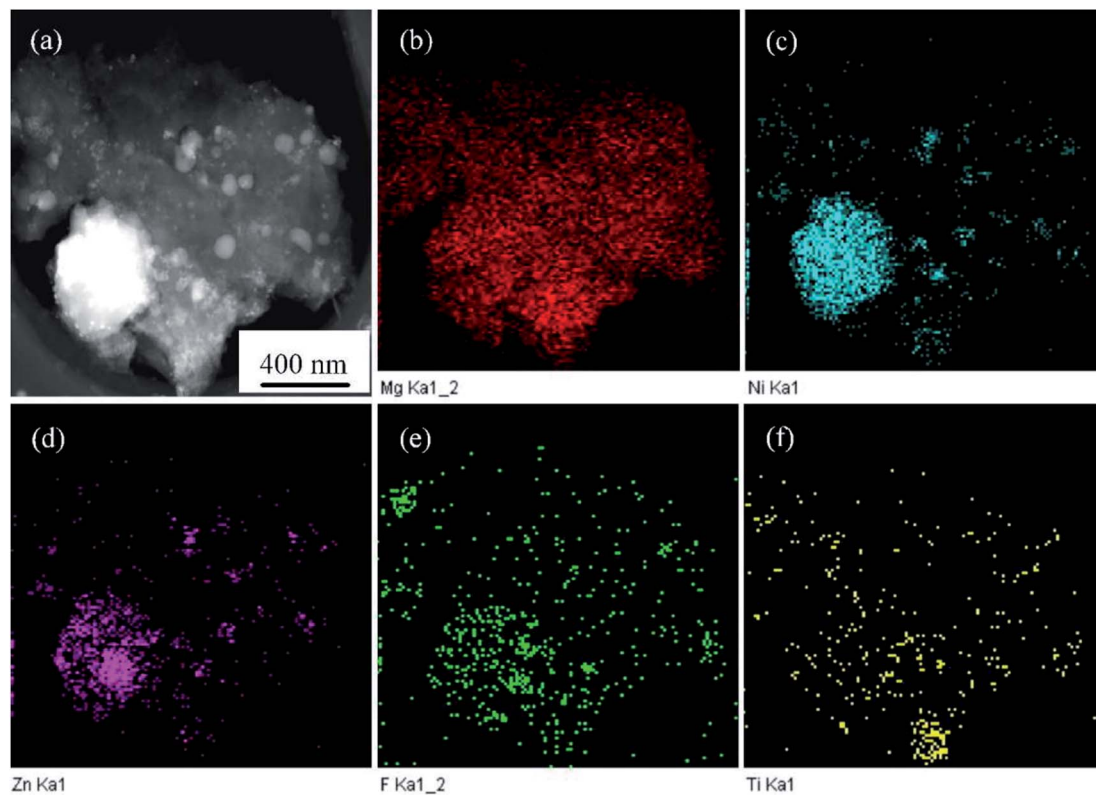


Fig. 3 FETEM micrographs and EDS mapping of the $\text{Mg}_{85}\text{Zn}_5\text{Ni}_{10}-4\text{TiF}_3$ alloy after hydrogen desorption cycles.

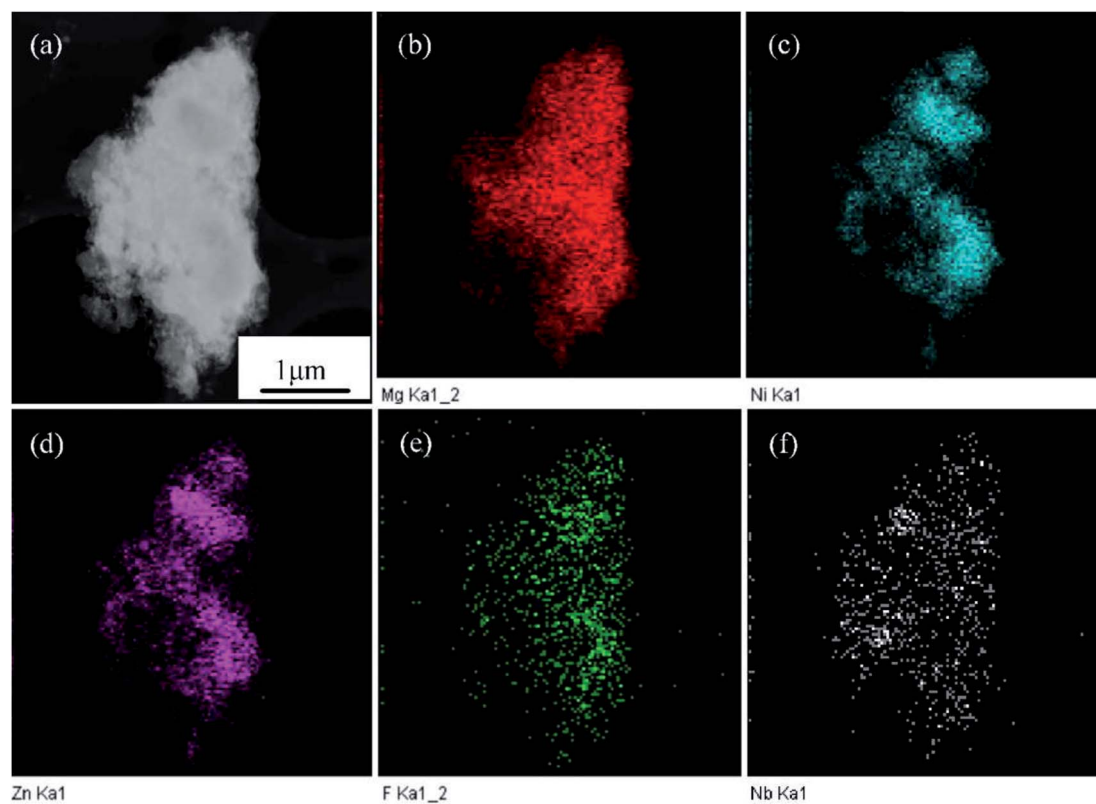


Fig. 4 FETEM micrographs and EDS mapping of the $\text{Mg}_{85}\text{Zn}_5\text{Ni}_{10}-4\text{NbF}_5$ alloy after hydrogen desorption cycles.



TiF₃ and NbF₅ are both present after hydrogenation and dehydrogenation cycles suggesting that they do not react with hydrogen or decompose after hydriding and dehydriding cycles.

Hydrogenation and dehydrogenation kinetics

With the aim to study the influence of different catalysts on hydrogenation kinetics of Mg₈₅Zn₅Ni₁₀, the hydrogen absorptions of the ball-milled Mg₈₅Zn₅Ni₁₀-4C (C = TiF₃, NbF₅) alloys were measured at a pressure of 3 MPa and at 360, 340, 320, 300, 280, 260, 240, 220, 200 and 150 °C, as represented in Fig. 5. We can observe that at the beginning of the hydrogenation process, the ball-milled Mg₈₅Zn₅Ni₁₀-4C (C = TiF₃, NbF₅) alloys have a very fast hydrogenation rate and the alloys need relatively long time to get saturated. This is because the hydride layer that is formed swiftly covers the particle surfaces and blocks the hydrogen diffusion into the alloys. For the convenience of comparison, the hydrogen absorption capacity at 600 s has been taken as the reference. According to Fig. 5, the C = TiF₃ alloy can absorb 4.404, 4.33, 4.238, 4.153, 4.117 wt% at 360, 340, 320, 300, 280 °C, respectively in 600 s. Simultaneously, the C = NbF₅ alloy can absorb 4.313, 4.244, 4.235, 4.197, 4.06 wt% at the same condition. Distinctly, the hydrogenation absorption rate within 600 s of C = TiF₃ alloy is a little faster than the C = NbF₅ alloy, also at relatively low temperatures. From Fig. 5(c) and (d), even at 150 °C, the C = TiF₃ alloy shows a faster absorption rate comparing with C = NbF₅ alloy. This explains that TiF₃ has

more effective catalytic effect than NbF₅. The ball-milled Mg₈₅Zn₅Ni₁₀-4C (C = TiF₃, NbF₅) alloys show very fast hydrogenation rate. This is probably due to the TiF₃ and NbF₅ catalysts promoting H₂ molecules to dissociate into H atoms and distribute on the surfaces of the Mg particles. Also, after ball milling with TiF₃ and NbF₅, the uniform mixing powders generated defects and cracks during the hydriding/dehydriding process, as illustrated in Fig. 6. These defects and cracks provide hydrogen diffusion channels and nucleation positions to form magnesium hydrides. As a comparison, the cracks formed on the C = TiF₃ alloy particles are evidently more than those on the C = NbF₅ alloy. This is the reason why the C = TiF₃ alloy has faster hydrogen absorption kinetics, even at relatively low temperatures.

The hydrogen desorptions of the ball-milled Mg₈₅Zn₅Ni₁₀-4C (C = TiF₃, NbF₅) alloys were tested to investigate the different catalytic effects between TiF₃ and NbF₅ on the hydrogen desorption kinetics, as depicted in Fig. 7. The hydrogen desorption from the alloys was tested at 360, 340, 320, 300 and 280 °C. Evidently, the temperature significantly affects the hydrogen desorption kinetics. The ball-milled Mg₈₅Zn₅Ni₁₀-4C (C = TiF₃, NbF₅) alloys have very fast desorption kinetics over 320 °C. The ball-milled Mg₈₅Zn₅Ni₁₀-4C (C = TiF₃, NbF₅) alloys could release all the hydrogen in less than 300 s at 360 °C, but took more than 30 minutes at 280 °C. According to Fig. 7, the time taken for releasing 4 wt% H₂ at 360, 340, 320, 300 and 280 °C is 102, 156, 318, 726 and 1836 s, respectively for the C =

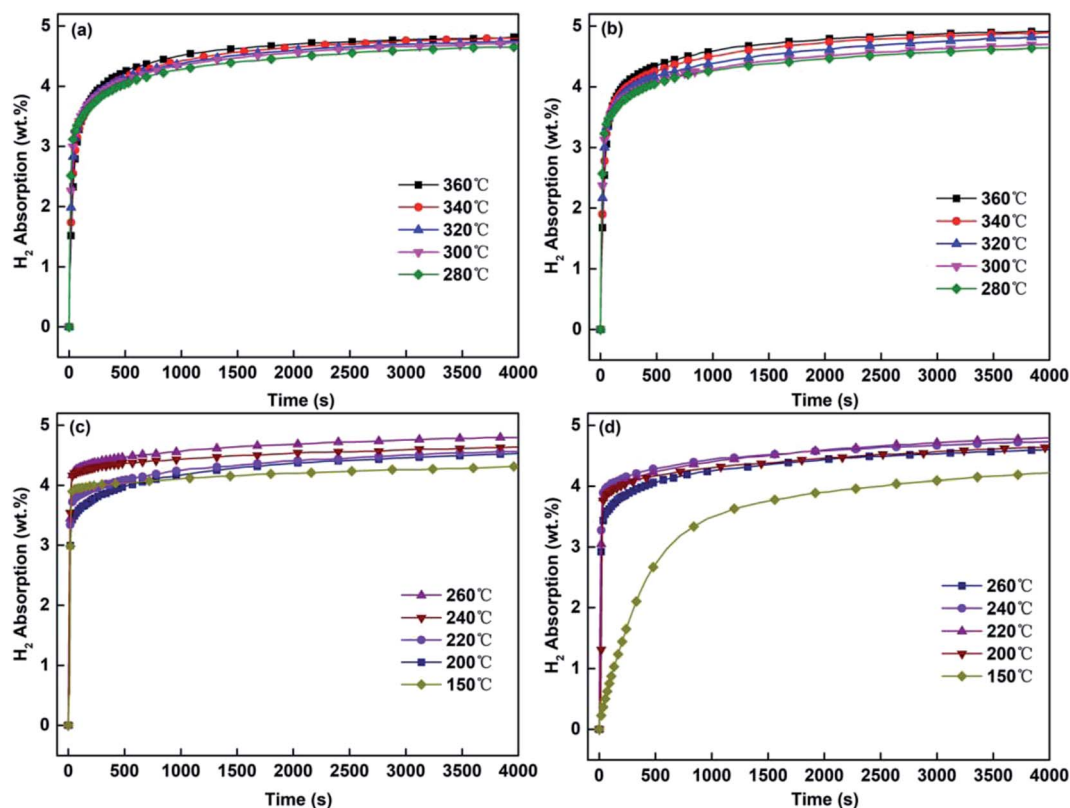


Fig. 5 Hydrogen absorption kinetic curves of the ball-milled Mg₈₅Zn₅Ni₁₀-4C (C = TiF₃, NbF₅) alloys at different temperatures: (a) and (c) C = TiF₃, (b) and (d) C = NbF₅.



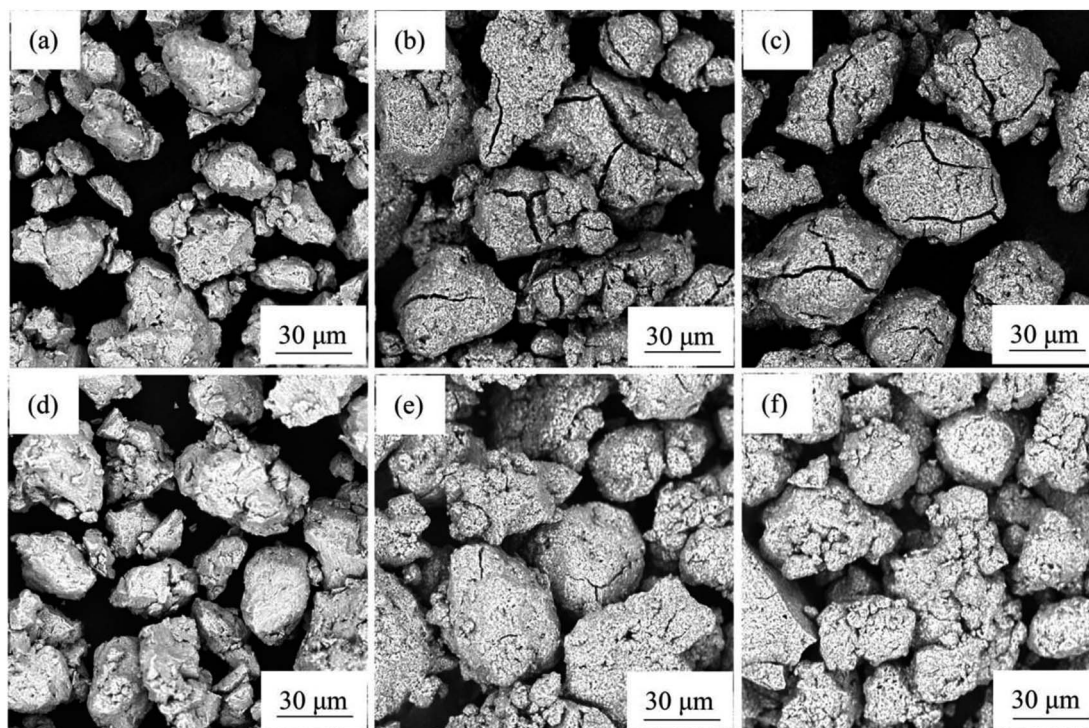


Fig. 6 SEM images of the ball-milled $\text{Mg}_{85}\text{Zn}_5\text{Ni}_{10}-4\text{C}$ ($\text{C} = \text{TiF}_3, \text{NbF}_5$) alloys: (a) $\text{C} = \text{TiF}_3$ alloy after ball milling, (b) $\text{C} = \text{TiF}_3$ alloy after dehydrogenation, (c) $\text{C} = \text{TiF}_3$ alloy after dehydrogenation, (d) $\text{C} = \text{NbF}_5$ alloy after ball milling, (e) $\text{C} = \text{NbF}_5$ alloy after hydrogenation, (f) $\text{C} = \text{NbF}_5$ alloy after dehydrogenation.

TiF_3 alloy, and 150, 222, 348, 756 and 1860 s, respectively for the $\text{C} = \text{NbF}_5$ alloy. This indicates the $\text{C} = \text{TiF}_3$ alloy has better desorption kinetics than $\text{C} = \text{NbF}_5$ alloy owing to the defects and cracks (Fig. 6(c) and (f)) formed on the particles which promote the hydrogen diffusion. Certainly, both catalysts have significant effects on the hydrogenation kinetics compared with the milled MgH_2 , which hardly decomposes at 300°C .⁴⁴

Hydrogen desorption property

To further study the different catalytic effects between TiF_3 and NbF_5 on hydrogen desorption property of $\text{Mg}_{85}\text{Zn}_5\text{Ni}_{10}$, the composites were characterized by DSC measurement as shown in Fig. 8. There is a big difference between the DSC curves of the ball-milled $\text{Mg}_{85}\text{Zn}_5\text{Ni}_{10}-4\text{C}$ ($\text{C} = \text{TiF}_3, \text{NbF}_5$) alloys, as seen in Fig. 8. There are two endothermic peaks in the curve of $\text{C} = \text{NbF}_5$ alloy at 228.84°C and 349.93°C . On the basis of XRD and TEM results, there are two reversible reactions in every hydrogenation and dehydrogenation reactions. The dehydrogenation reactions are $\text{MgH}_2 \rightarrow \text{Mg} + \text{H}_2$ and $\text{Mg}_2\text{NiH}_4 \rightarrow \text{Mg}_2\text{Ni} + \text{H}_2$. Therefore, the peak at 228.84°C belongs to the endothermic peak of Mg_2NiH_4 and the peak at 349.93°C corresponds to MgH_2 .^{43,45–47} However, for the $\text{C} = \text{TiF}_3$ alloy, there seems to be only one endothermic peak at 256.88°C in the DSC curve. This indicates that the catalyst TiF_3 strongly decreases the endothermic peak temperature of MgH_2 , and even causes the two peaks of Mg_2NiH_4 and MgH_2 to coincide. It illustrates that the reaction for MgH_2 decomposition becomes more easy by adding TiF_3 . Conversely, there is no such significant catalytic effect by

NbF_5 . This also proves that TiF_3 improves the hydrogen desorption property of $\text{Mg}_{85}\text{Zn}_5\text{Ni}_{10}$ more effectively than NbF_5 . This result is in line with previous discussions of hydrogenation and dehydrogenation kinetics. Moreover, the onset temperatures of dehydrogenations are 218.63 and 210.08°C of $\text{C} = \text{TiF}_3$ and NbF_5 alloys, respectively.

Hydrogenation and dehydrogenation cyclic stability

Fig. 9 and 10 depict the hydrogen absorbing and desorbing cyclic stability curves of the ball-milled $\text{Mg}_{85}\text{Zn}_5\text{Ni}_{10}-4\text{C}$ ($\text{C} = \text{TiF}_3, \text{NbF}_5$) alloys at 360°C . According to Fig. 9 and 10, basically there is no change of hydrogen absorption and desorption capacities for both $\text{C} = \text{TiF}_3$ alloy and $\text{C} = \text{NbF}_5$ alloy after 15 cycles. It is remarkable that the hydrogenation rate of first cycle for the ball-milled $\text{Mg}_{85}\text{Zn}_5\text{Ni}_{10}-4\text{C}$ ($\text{C} = \text{TiF}_3, \text{NbF}_5$) alloys is quite slow owing to a long process of complete activation of the alloys. However, after the second cycle, the hydrogenation and dehydrogenation rates are significantly accelerated. Subsequently, with the increase of cycle times, the hydrogenation and dehydrogenation rates gradually improve and show good kinetics. This is because defects and cracks are generated during the hydrogenation and dehydrogenation cycles. These defects and cracks can provide more hydrogen diffusion channels and nucleation positions for Mg hydrides which was discussed previously. Therefore, the hydrogen absorption and desorption cyclic curves are almost identical. Also, there is no capacity loss even after 30 hydrogenation/dehydrogenation cycles. On the basis of Fig. 9 and 10, the ball-milled



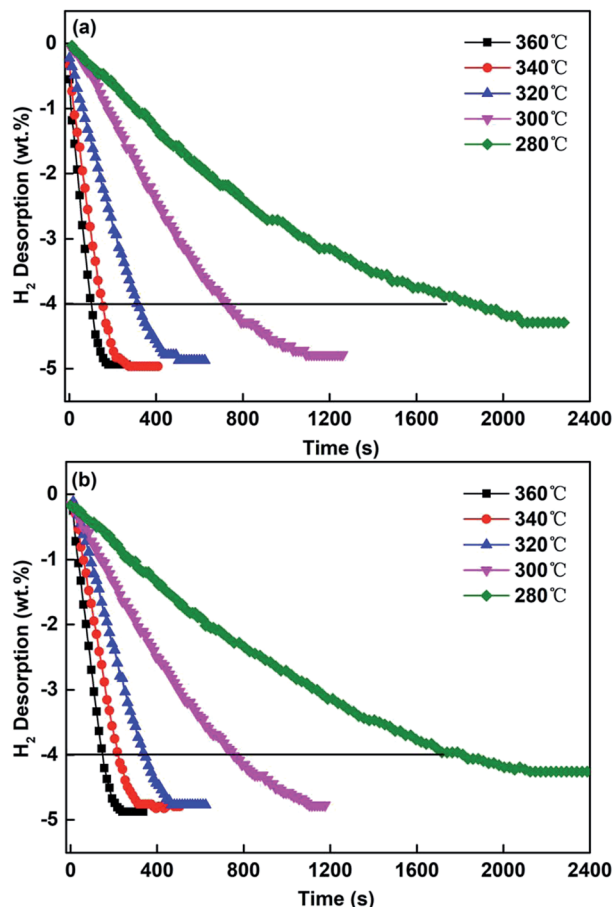


Fig. 7 Hydrogen desorption kinetic curves of the ball-milled $\text{Mg}_{85}\text{Zn}_5\text{Ni}_{10}\text{-4C}$ ($\text{C} = \text{TiF}_3, \text{NbF}_5$) alloys at different temperatures: (a) $\text{C} = \text{TiF}_3$, (b) $\text{C} = \text{NbF}_5$.

$\text{Mg}_{85}\text{Zn}_5\text{Ni}_{10}\text{-4C}$ ($\text{C} = \text{TiF}_3, \text{NbF}_5$) alloys reveal good hydrogenation and dehydrogenation cyclic stability. Furthermore, the capacity without any loss indicates that there is no other stable hydride formation during the hydrogenation/dehydrogenation

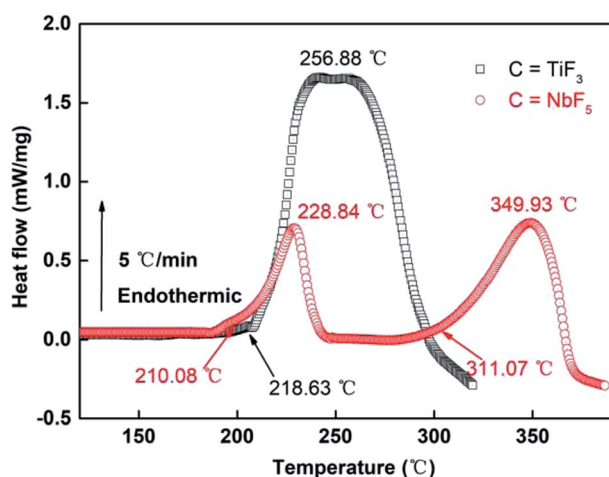


Fig. 8 DSC curves of the desorption process of the ball-milled $\text{Mg}_{85}\text{Zn}_5\text{Ni}_{10}\text{-4C}$ ($\text{C} = \text{TiF}_3, \text{NbF}_5$) alloys.

process. Subsequently, the decomposition of $\text{TiF}_3/\text{NbF}_5$ and formation of $\text{TiH}_2/\text{NbH}_2$ is always accompanied by the loss of capacity owing to the formation of TiH_2 . $\text{TiH}_2/\text{NbH}_2$ cannot release hydrogen during dehydrogenation of MgH_2 .^{48–50} Therefore, this also proves that both TiF_3 and NbF_5 exist stably in the ball-milled $\text{Mg}_{85}\text{Zn}_5\text{Ni}_{10}\text{-4C}$ ($\text{C} = \text{TiF}_3, \text{NbF}_5$) alloys.

Hydrogen desorption activation energy

In order to further study the catalytic mechanism of the differences between TiF_3 and NbF_5 , the dehydrogenation activation energy of the $\text{Mg}_{85}\text{Zn}_5\text{Ni}_{10}\text{-4C}$ ($\text{C} = \text{TiF}_3, \text{NbF}_5$) alloys is estimated by Arrhenius method. As a general rule, in a gas–solid reaction, the total energy barrier which is to be crossed determines the activation energy. The energy barrier of H_2 released from MgH_2 is the leading cause which may explain the dehydrogenation rate.³⁴ During hydrogenation, the activation energy is considered to be relative to the total energy barrier. As we know, the dehydrogenation reaction is accomplished by nucleation and growth processes. In addition, the Johnson–Mehl–Avrami (JMA) model always simulates the nucleation and

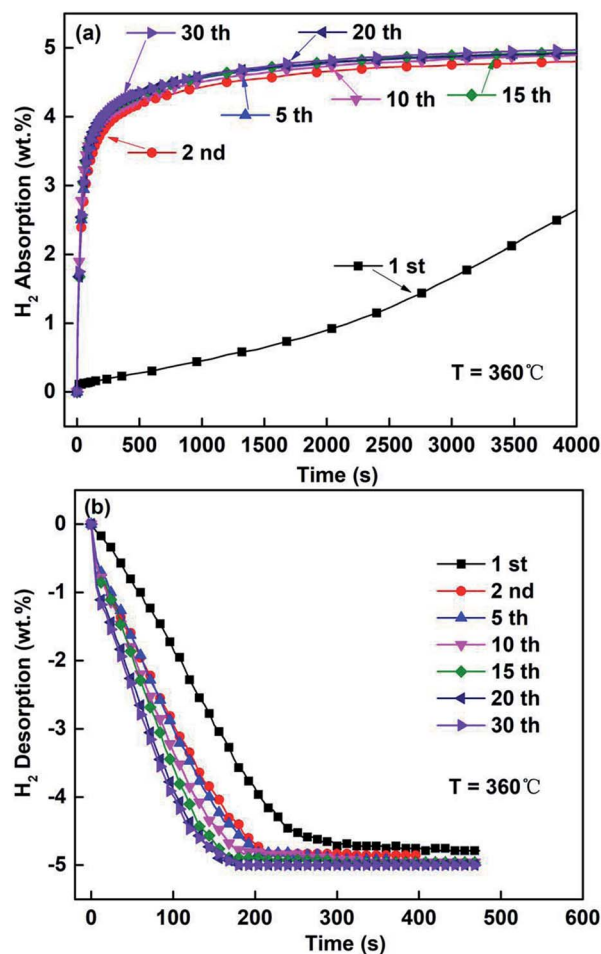


Fig. 9 Hydrogenation/dehydrogenation cycling curves of $\text{Mg}_{85}\text{Zn}_5\text{Ni}_{10}\text{-4TiF}_3$ alloy at 360 °C: (a) hydrogenation cycles, (b) dehydrogenation cycles.



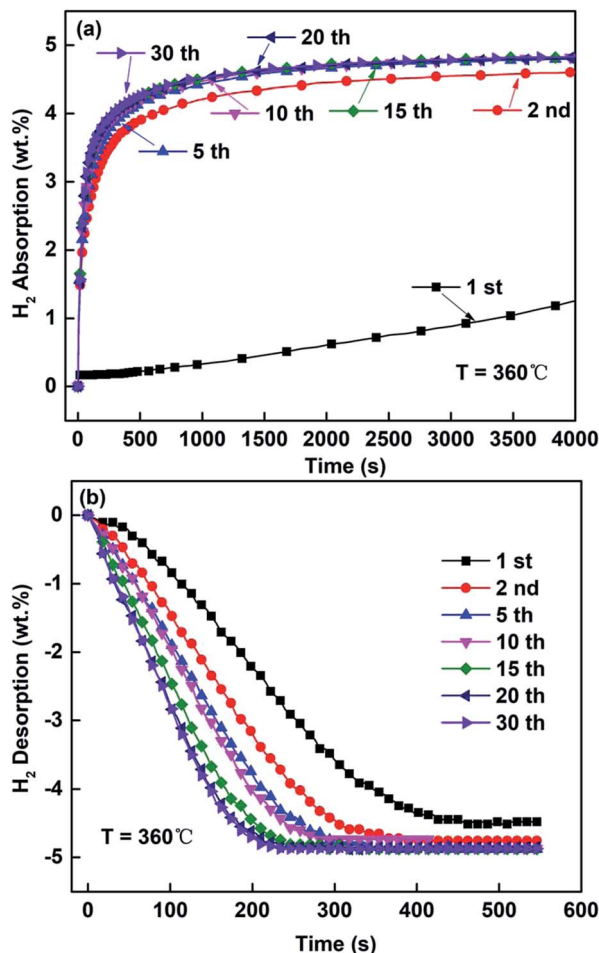


Fig. 10 Hydrogenation/dehydrogenation cycling curves of $\text{Mg}_{85}\text{Zn}_5\text{-Ni}_{10}\text{-4NbF}_5$ alloy at 360 °C: (a) hydrogenation cycles, (b) dehydrogenation cycles.

growth processes during hydrogen desorption, which is represented by the following equation:⁵¹

$$\ln[-\ln(1 - \alpha)] = \eta \ln k + \eta \ln t \quad (1)$$

where α , k and η represent the reaction fraction at time t , an effective kinetic parameter, and the Avrami exponent reaction order, respectively. Fig. 11 expresses the linear plots of $\ln[-\ln(1 - \alpha)]$ vs. the $\ln t$. Evidently, the JMA plots described in Fig. 11 are nearly linear, illustrating that dehydriding reactions of the samples follow instantaneous nucleation followed by interface controlled-three-dimensional growth process.⁵² According to the slope and intercept of the linear fitting, η and $\eta \ln k$ values at each temperature can be calculated. On the basis of η and $\eta \ln k$ values, the rate constant k is calculated, then the activation energy (E_a) for dehydrogenation can be computed from the following Arrhenius equation:^{53,54}

$$k = A \exp(-E_a/RT) \quad (2)$$

where, A , R and T represent a temperature independent coefficient, universal gas constant and the absolute temperature,

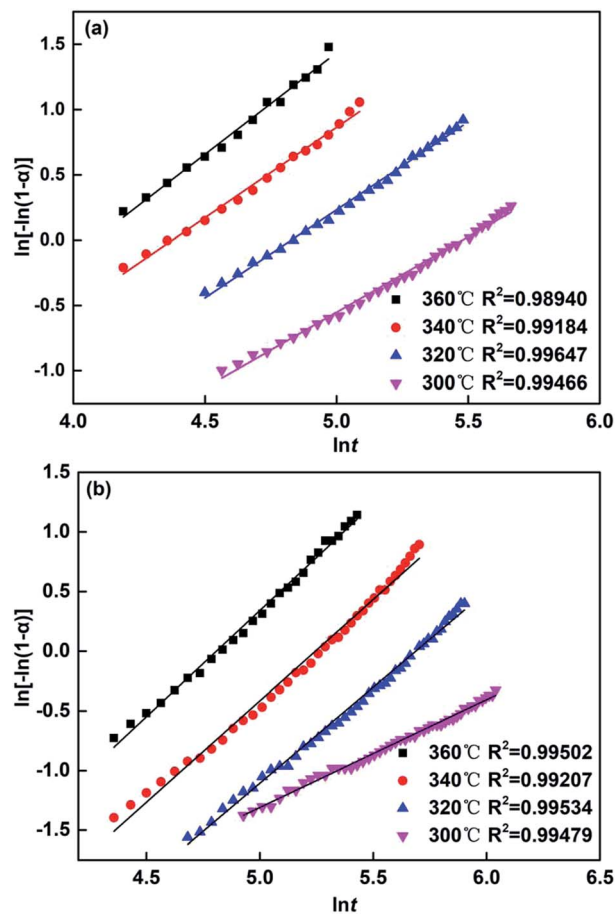


Fig. 11 JMA graphs of the as-milled and ball-milled $\text{Mg}_{85}\text{Zn}_5\text{Ni}_{10}\text{-4C}$ ($\text{C} = \text{TiF}_3$, NbF_5) alloys at different temperatures: (a) $\text{C} = \text{TiF}_3$, (b) $\text{C} = \text{NbF}_5$.

respectively. The Arrhenius plots for the dehydrogenation kinetics are described in Fig. 12. Accordingly, on the basis of the slopes of these plots, the activation energy, E_a (de), can be calculated. The E_a (de) values of the ball-milled $\text{Mg}_{85}\text{Zn}_5\text{Ni}_{10}\text{-4C}$ ($\text{C} = \text{TiF}_3$, NbF_5) alloys are 75.514 and 82.367 $\text{kJ mol}^{-1} \text{H}_2$, respectively, and are listed in Table 1. Clearly, the E_a (de) of $\text{C} = \text{TiF}_3$ alloy is much lower than that of the $\text{C} = \text{NbF}_5$ alloy. In this study, the E_a (de) value of ball-milled $\text{Mg}_{85}\text{Zn}_5\text{Ni}_{10}$ is calculated to be 109.83 $\text{kJ mol}^{-1} \text{H}_2$, suggesting that both catalysts remarkably decreased the dehydriding activation energy when compared with the E_a (de) value of pure milled MgH_2 (158.5 $\text{kJ mol}^{-1} \text{H}_2$).⁵⁵

Hydrogen storage thermodynamics

The pressure-composition Isotherms (PCI) tests were measured at 360, 340 and 320 °C for the sake of studying the influence of different catalysts on the hydrogen storage thermodynamics of the ball-milled $\text{Mg}_{85}\text{Zn}_5\text{Ni}_{10}\text{-4C}$ ($\text{C} = \text{TiF}_3$, NbF_5) alloy. The PCI curves are represented in Fig. 13. Evidently, in each PCI curves there are two distinct plateaus. The lower pressure plateau belongs to MgH_2 , and the higher one is the pressure plateau of Mg_2NiH_4 according to the reported results for Mg-10Ni-xMm

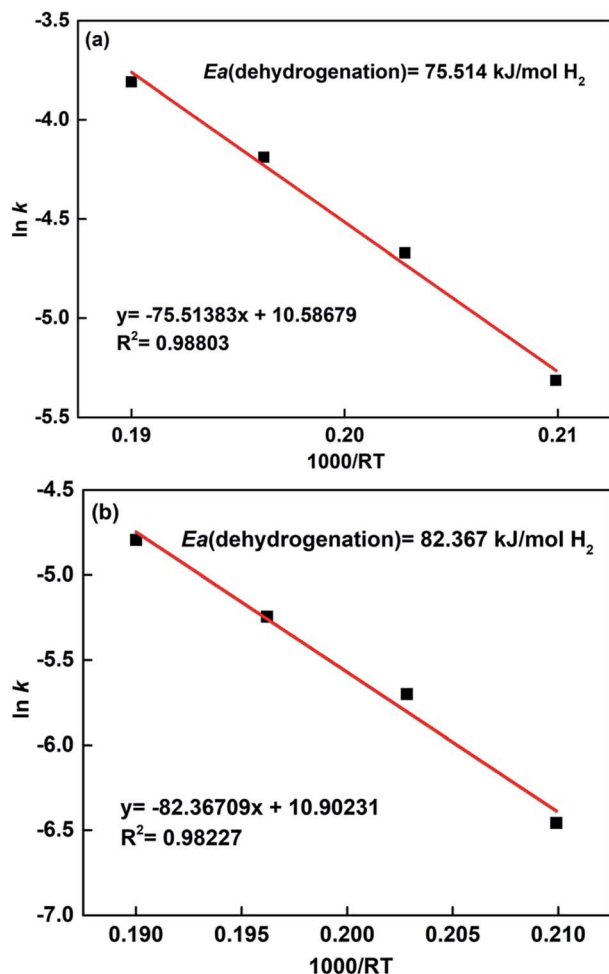


Fig. 12 P–C–I curves of the as-milled of the ball-milled $\text{Mg}_{85}\text{Zn}_5\text{Ni}_{10}-4\text{C}$ ($\text{C} = \text{TiF}_3, \text{NbF}_5$) alloys at different temperatures: (a) $\text{C} = \text{TiF}_3$, (b) $\text{C} = \text{NbF}_5$.

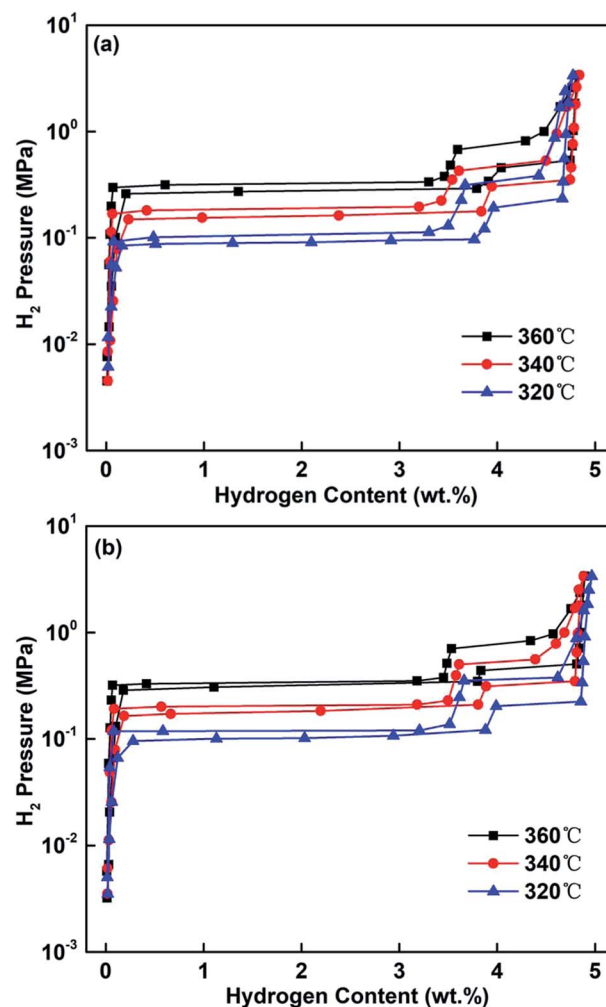


Fig. 13 P–C–I curves of the as-milled of the ball-milled $\text{Mg}_{85}\text{Zn}_5\text{Ni}_{10}-4\text{C}$ ($\text{C} = \text{TiF}_3, \text{NbF}_5$) alloys at different temperatures: (a) $\text{C} = \text{TiF}_3$, (b) $\text{C} = \text{NbF}_5$.

alloy.⁵⁶ All the curves exhibit flat plateaus. On the basis of the plateau pressures in PCI curves, both enthalpy change ΔH and entropy change ΔS can be derived from the Van't Hoff equation:⁵⁷

$$\ln[P(\text{H}_2)/P_0] = \Delta H/(RT) - \Delta S/R \quad (3)$$

where, $P(\text{H}_2)$, P_0 , T and R represent the equilibrium hydrogen gas pressure, the standard atmospheric pressure, the sample temperature and the gas constant, respectively. Fig. 14 shows the Van't Hoff plots and the enthalpy value (ΔH) and entropy value (ΔS) of the ball-milled $\text{Mg}_{85}\text{Zn}_5\text{Ni}_{10}-4\text{C}$ ($\text{C} = \text{TiF}_3, \text{NbF}_5$) alloy. Therefore, the thermodynamic parameters can be easily

calculated by intercepts and slopes of the Van't Hoff plots which are listed in Table 1. The calculations reveal that the hydrogen absorption/desorption ΔH and ΔS of the $\text{C} = \text{TiF}_3$ alloy are smaller than of the $\text{C} = \text{NbF}_5$ alloy indicating that TiF_3 is more effective than NbF_5 as a catalyst to improve the hydrogen storage thermodynamics of $\text{Mg}_{85}\text{Zn}_5\text{Ni}_{10}$. Meanwhile, the hydrogen absorption/desorption ΔH and ΔS of ball-milled $\text{Mg}_{85}\text{Zn}_5\text{Ni}_{10}-4\text{C}$ ($\text{C} = \text{TiF}_3, \text{NbF}_5$) alloys are smaller than those of ball-milled $\text{Mg}_{85}\text{Zn}_5\text{Ni}_{10}$ alloy, suggesting both TiF_3 and NbF_5 are helpful to ameliorate the thermodynamics of $\text{Mg}_{85}\text{Zn}_5\text{Ni}_{10}$.

Table 1 Hydrogen desorption activation energy (E_a (de)), enthalpy change (ΔH) and entropy change (ΔS) of the ball-milled $\text{Mg}_{85}\text{Zn}_5\text{Ni}_{10}-4\text{C}$ ($\text{C} = \text{TiF}_3, \text{NbF}_5$, none) alloy

$\text{Mg}_{85}\text{Zn}_5\text{Ni}_{10}-4\text{C}$ alloys	E_a (de) (kJ mol^{-1})	ΔH_{ab} (kJ mol^{-1})	ΔS_{ab} ($\text{J mol}^{-1} \text{K}^{-1}$)	ΔH_{de} (kJ mol^{-1})	ΔS_{de} ($\text{J mol}^{-1} \text{K}^{-1}$)
$\text{C} = \text{TiF}_3$	75.514	−70.100	−122.473	80.054	137.781
$\text{C} = \text{NbF}_5$	82.367	−75.869	−128.945	79.005	132.683
$\text{C} = \text{none}$	109.830	−82.446	−140.628	86.187	146.114



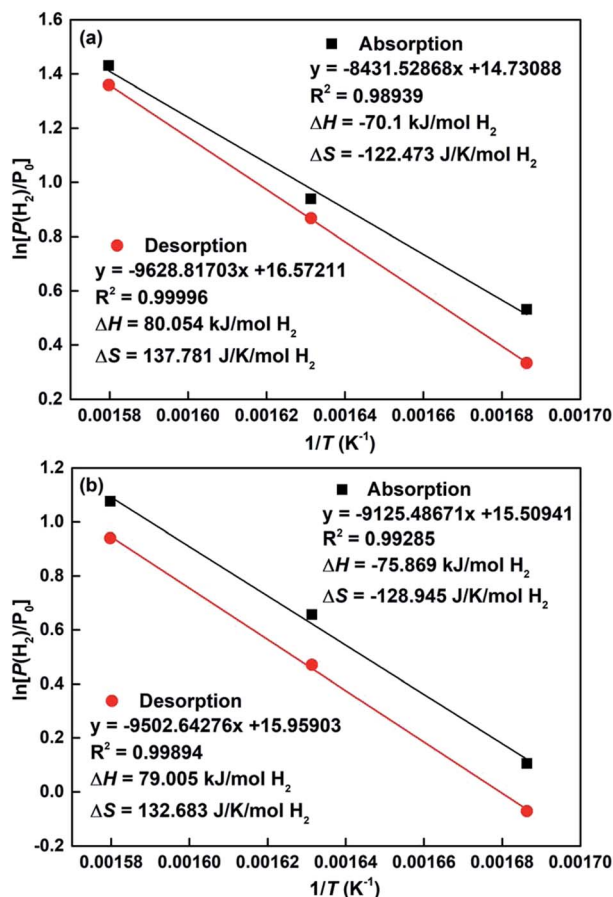


Fig. 14 Van't Hoff plots of the as-milled of the ball-milled $\text{Mg}_{85}\text{Zn}_5\text{Ni}_{10}-4\text{C}$ ($\text{C} = \text{TiF}_3$, NbF_5) alloys at different temperatures: (a) $\text{C} = \text{TiF}_3$, (b) $\text{C} = \text{NbF}_5$.

Conclusions

In this investigation, as-milled $\text{Mg}_{85}\text{Zn}_5\text{Ni}_{10}-4\text{C}$ ($\text{C} = \text{TiF}_3$, NbF_5) specimens have been prepared successfully *via* ball milling. The different influences between the catalysts TiF_3 and NbF_5 on the microstructure and hydrogen storage properties were studied. The main conclusions drawn are as follows:

(1) After 5 h ball milling, and 30 hydrogenation/dehydrogenation cycles, the catalysts TiF_3 and NbF_5 always exist in the $\text{Mg}_{85}\text{Zn}_5\text{Ni}_{10}-4\text{C}$ ($\text{C} = \text{TiF}_3$, NbF_5) composites, indicating that both TiF_3 and NbF_5 do not decompose and have a good stability.

(2) The $\text{C} = \text{TiF}_3$ alloy possesses a faster hydrogen absorption/desorption rate than the $\text{C} = \text{NbF}_5$ alloy. The dehydrogenation activation energy values calculated by Arrhenius equation of the as-milled $\text{Mg}_{85}\text{Zn}_5\text{Ni}_{10}-4\text{C}$ ($\text{C} = \text{TiF}_3$, NbF_5) alloys are 75.514 and 82.367 $\text{kJ mol}^{-1} \text{H}_2$, respectively, while the value of ball-milled $\text{Mg}_{85}\text{Zn}_5\text{Ni}_{10}$ alloy is 109.830 $\text{kJ mol}^{-1} \text{H}_2$, indicating that the catalysts TiF_3 and NbF_5 visibly reduce the dehydrogenation activation energy and effectively improve the hydrogen absorption/desorption kinetics.

(3) Compared with the ball-milled $\text{Mg}_{85}\text{Zn}_5\text{Ni}_{10}$ alloy, the composites catalyzed by TiF_3 and NbF_5 possess lower

thermodynamic parameters (ΔH and ΔS), suggesting that TiF_3 and NbF_5 can significantly ameliorate the hydrogen storage thermodynamics.

(4) TiF_3 has a better effect to generate more defects and cracks during the hydriding/dehydriding process than NbF_5 , which is responsible for the faster hydrogen absorption/desorption rate. During hydrogenation and dehydrogenation, defects and cracks existing on alloy particles play an effective and important role in increasing the hydrogen absorption and desorption rates. TiF_3 has a better catalytic effect on the hydrogen storage property of $\text{Mg}_{85}\text{Zn}_5\text{Ni}_{10}$ than NbF_5 .

Conflicts of interest

There are no conflicts to declare.

Acknowledgements

This study is financially supported by the National Natural Science Foundations of China (51761032, 51471054 and 51871125).

References

- W. J. Song, J. S. Li, T. B. Zhang, X. J. Hou and H. C. Kou, *RSC Adv.*, 2015, 5, 54258–54265.
- N. Juahir, N. S. Mustafa, A. M. Sinin and M. Ismail, *RSC Adv.*, 2015, 5, 60983–60989.
- R. F. Bill, D. Reed, D. Book and P. A. Anderson, *J. Alloys Compd.*, 2015, 645, S96–S99.
- L. Z. Ouyang, Z. J. Cao, H. Wang, J. W. Liu, D. L. Sun, Q. A. Zhang and M. Zhu, *J. Alloys Compd.*, 2014, 586(6), 113–117.
- Y. J. Yang, Y. F. Liu, Y. Zhang, Y. Li, M. X. Gao and H. G. Pan, *J. Alloys Compd.*, 2014, 585, 674–680.
- L. Z. Ouyang, J. Tang, Y. Zhao, H. Wang, X. Yao, J. Liu, J. Zou and M. Zhu, *Sci. Rep.*, 2015, 5, 10776.
- Z. M. Yuan, W. Zhang, P. L. Zhang, Y. H. Zhang, W. G. Bu, S. H. Guo and D. L. Zhao, *RSC Adv.*, 2017, 7, 56365–56374.
- Y. H. Zhang, M. Ji, Z. M. Yuan, W. G. Bu, Y. Qi and S. H. Guo, *RSC Adv.*, 2017, 7, 37689–37698.
- Y. F. Liu, H. G. Pan, M. X. Gao, R. Li and Y. Q. Lei, *J. Alloys Compd.*, 2004, 376, 296–303.
- Y. H. Zhang, P. P. Wang, W. G. Bu, Z. M. Yuan, Y. Qi and S. H. Guo, *RSC Adv.*, 2018, 8, 23353–23363.
- Y. F. Zhu, H. G. Pan, M. X. Gao, J. X. Ma, S. Q. Li and Q. D. Wang, *Int. J. Hydrogen Energy*, 2002, 27, 287–293.
- M. Chourashiya, D. C. Yang, C. N. Park and C. J. Park, *Int. J. Hydrogen Energy*, 2012, 37, 4238–4245.
- Y. Bai, C. Wu, F. Wu, J. H. Yang, L. L. Zhao, F. Long and B. L. Yi, *Int. J. Hydrogen Energy*, 2012, 37, 12973–12979.
- H. Wang, A. K. Prasad and S. G. Advani, *Int. J. Hydrogen Energy*, 2012, 37, 290–298.
- Y. F. Liu, H. F. Du, X. Zhang, Y. X. Yang, M. X. Gao and H. G. Pan, *Chem. Commun.*, 2015, 52, 705–708.
- H. J. Lin, J. Matsuda, H. W. Li, M. Zhu and E. Akiba, *J. Alloys Compd.*, 2015, 645, S392–S396.



- 17 D. F. Wu, L. Z. Ouyang, C. Wu, H. Wang, J. W. Liu, L. X. Sun and M. Zhu, *J. Alloys Compd.*, 2015, **642**, 180–184.
- 18 X. L. Luo, D. M. Grant and G. S. Walker, *J. Alloys Compd.*, 2015, **645**, S23–S26.
- 19 H. Wang, H. J. Lin, W. T. Cai, L. Z. Ouyang and M. Zhu, *J. Alloys Compd.*, 2016, **658**, 280–300.
- 20 D. Milcius, J. Grbovic-Novakovic, R. Zostautiene, M. Lelis, D. Girdzevicius and M. Urbonavicius, *J. Alloys Compd.*, 2015, **647**, 790–796.
- 21 I. E. Malka, T. Czujko and J. Bystrzycki, *Int. J. Hydrogen Energy*, 2010, **35**, 1706–1712.
- 22 F. Y. Cheng, Z. L. Tao, J. Liang and J. Chen, *Chem. Commun.*, 2012, **48**, 7334–7343.
- 23 J. J. Reilly Jr and R. H. Wiswall Jr, *J. Inorg. Chem.*, 1968, **7**, 2254–2256.
- 24 E. Akiba, K. Nomura, S. Ono and S. Suda, *Int. J. Hydrogen Energy*, 1982, **7**, 787–791.
- 25 T. Fujimoto, S. Ogawa, T. Kanai, N. Uchiyama, T. Yoshida and S. Yagi, *Int. J. Hydrogen Energy*, 2015, **40**, 11890–11894.
- 26 T. Liu, T. W. Zhang, X. Z. Zhang and X. G. Li, *Int. J. Hydrogen Energy*, 2011, **36**, 3515–3520.
- 27 J. Y. Wang, C. Y. Wu, J. K. Nieh, H. C. Lin, K. M. Lin and H. Y. Bor, *Int. J. Hydrogen Energy*, 2010, **35**, 1250–1256.
- 28 J. J. Reilly Jr and R. H. Wiswall Jr, *J. Inorg. Chem.*, 1967, **6**, 2220–2223.
- 29 K. I. Kim and T. W. Hong, *Korean J. Met Mater.*, 2011, **49**, 264–269.
- 30 Z. N. Li, X. P. Liu, Z. Huang, L. J. Jiang and S. M. Wang, *Rare Met.*, 2006, **25**, 247–251.
- 31 M. Lucaci, A. R. Biris, R. L. Orban, G. B. Sbarcea and V. Tsakiris, *J. Alloys Compd.*, 2009, **488**, 163–168.
- 32 T. Yang, Z. M. Yuan, W. G. Bu, Z. C. Jia, Y. Qi and Y. H. Zhang, *Int. J. Hydrogen Energy*, 2016, **41**, 2689–2699.
- 33 Z. M. Yuan, T. Yang, W. G. Bu, H. W. Shang, Y. Qi and Y. H. Zhang, *Int. J. Hydrogen Energy*, 2016, **41**, 5994–6003.
- 34 Y. H. Zhang, G. Huang, Z. M. Yuan, H. W. Shang, Y. Qi and S. H. Guo, *Mater. Sci. Eng., B*, 2017, **225**, 1–9.
- 35 T. Spassov, P. Delchev, P. Madjarov, M. Spassova and T. S. Himitliiska, *J. Alloys Compd.*, 2010, **495**, 149–153.
- 36 S. Long, J. X. Zou, X. Chen, X. Q. Zeng and W. J. Ding, *J. Alloys Compd.*, 2014, **615**, S684–S688.
- 37 J. Z. Song, S. M. Han and R. D. Fu, *Mater. Sci. Eng., B*, 2014, **188**, 114–118.
- 38 Y. J. Kwak, S. H. Lee, D. R. Mumm and M. Y. Song, *Int. J. Hydrogen Energy*, 2015, **40**, 11908–11916.
- 39 L. P. Ma, P. Wang and H. M. Cheng, *J. Alloys Compd.*, 2007, **432**, L1–L4.
- 40 S. K. Peng, X. Z. Xiao, R. J. Xu, L. Li, F. Wu, S. Q. Li, Q. D. Wang and L. X. Chen, *Trans. Nonferrous Met. Soc. China*, 2010, **20**, 1879–1884.
- 41 A. R. Yavari, A. LeMoulec, F. R. de Castro, S. Deledda, O. Friedrichs, W. J. Botta, G. Vaughan, T. Klassen, A. Fernandez and Å. Kvik, *Scr. Mater.*, 2005, **52**, 719–724.
- 42 S. H. Lee, Y. J. Kwak, H. R. Park and M. Y. Song, *Int. J. Hydrogen Energy*, 2014, **39**, 16486–16492.
- 43 N. Recham, V. V. Bhat, M. Kandavel, L. Aymard, J. M. Tarascon and A. Rougier, *J. Alloys Compd.*, 2008, **464**, 377–382.
- 44 R. K. Singh, T. Sadhasivam, G. I. Sheeja, P. Singh and O. N. Srivastava, *Int. J. Hydrogen Energy*, 2013, **38**, 6221–6225.
- 45 M. Ismail, Y. Zhao, X. B. Yu and S. X. Dou, *Int. J. Hydrogen Energy*, 2012, **37**, 8395–8401.
- 46 S. S. Liu, L. X. Sun, F. Xu, J. Zhang, Z. Cao and Y. L. Liu, *Int. J. Hydrogen Energy*, 2011, **36**, 11785–11793.
- 47 N. S. Mustafa, M. C. Law and M. Ismail, *Mater. Today*, 2016, **3**, S96–S103.
- 48 R. R. Shahi, A. Bhatnagar, S. K. Pandey, V. Dixit and O. N. Srivastava, *Int. J. Hydrogen Energy*, 2014, **39**, 14255–14261.
- 49 A. Grzech, U. Lafont, P. C. M. M. Magusin and F. M. Mulder, *J. Phys. Chem. C*, 2012, **116**, 26027–26035.
- 50 Y. J. Kwak, S. H. Lee, D. R. Mumm and M. Y. Song, *Int. J. Hydrogen Energy*, 2015, **40**, 11908–11916.
- 51 M. Pourabdoli, S. Raygan, H. Abdizadeh and D. Uner, *Int. J. Hydrogen Energy*, 2013, **38**, 11910–11919.
- 52 T. Czujko, R. A. Varin, C. Chiu and Z. Wronski, *J. Alloys Compd.*, 2006, **414**, 240–247.
- 53 T. Liu, Y. R. Cao, C. G. Qin, W. S. Chou and X. G. Li, *J. Power Sources*, 2014, **246**, 277–282.
- 54 T. Kimura, H. Miyaoka, T. Ichikawa and Y. Kojima, *Int. J. Hydrogen Energy*, 2013, **38**, 13728–13733.
- 55 J. F. Mao, Z. P. Guo, X. B. Yu, H. K. Liu, Z. Wu and J. Ni, *Int. J. Hydrogen Energy*, 2010, **35**, 4569–4575.
- 56 J. G. Yuan, N. Xing and Y. Wu, *Int. J. Hydrogen Energy*, 2017, **42**, 6118–6126.
- 57 H. Falahati and D. P. J. Barz, *Int. J. Hydrogen Energy*, 2013, **38**, 8838–8851.

